Liu et al. Nanoscale Res Lett (2021) 16:66
https://doi.org/10.1186/s11671-021-03526-x

Nanoscale Research Letters

NANO EXPRESS

Open Access

Molecular Dynamics Simulation on Cutting Mechanism in the Hybrid Machining Process of Single-Crystal Silicon

Changlin Liu, Wenbin He, Jianning Chu, Jianguo Zhang, Xiao Chen, Junfeng Xiao and Jianfeng Xu*

Abstract

In this paper, molecular dynamics simulations are carried out to investigate the cutting mechanism during the hybrid machining process combined the thermal and vibration assistants. A modified cutting model is applied to study the material removal behavior and subsurface damage formation in one vibration cycle. The results indicate that during the hybrid machining process, the dominant material removal mechanism could transform from extrusion to shearing in a single vibration cycle. With an increase of the cutting temperature, the generation and propagation of cracks are effectively suppressed while the swelling appears when the dominant material removal mechanism becomes shearing. The formation mechanism of the subsurface damage in one vibration cycle can be distinct according to the stress distribution. Moreover, the generation of the vacancies in workpiece becomes apparent with increasing temperature, which is an important phenomenon in hybrid machining process.

Keywords: Molecular dynamics simulation, Single-crystal silicon, Hybrid machining process, Cutting mechanism

Introduction

Single-crystal silicon is an important semiconductor material, which has been widely used in infrared optics, microelectronics, and optoelectronics systems owing to its excellent optical and mechanical properties [1, 2]. However, due to the hardness and brittleness nature of single-crystal silicon, microscopic brittle fracture and subsurface damage can be generated during mechanical machining. During micro-milling process, machining-induced interior type edge chipping defects can be generated in workpiece [3]. In single-crystal diamond cutting (SPDT) machining, a damaged layer ranges from 200 to 600 nm can be formed depending on processing parameters [4, 5]. Although the subsurface damage layer can be decreased to about 50 nm by grinding and polishing. The machining efficiency and ability in fabricating complex structures are limited. To overcome these problems, various assistive machining technologies have been proposed and tested. In particular, the thermal assisted cutting (TAC) [6] and vibration assisted cutting (VAC) [7] have attracted widespread attention as its extraordinary cutting performance.

For brittle materials like single-crystal silicon, the brittle-to-ductile transition can be promoted when the machining temperature is increased. During TAC process, the silicon workpiece is thermally softened, which causes the decrease of the cutting forces [8] and specific cutting energy [9, 10]. Meanwhile, the annealing of the high-pressure phases into cubic silicon phase become apparent when the machining temperature is increased [11]. With appropriate selection of the machining parameters, desired machined surface with high phase purity and low subsurface damage can be achieved by TAC [12–14]. In addition to TAC, the vibration assisted cutting (VAC) is another promoting method to achieve high-quality surface on single-crystal silicon. This technique has been applied in the manufacturing industry

*Correspondence: jfxu@hust.edu.cn
State Key Laboratory of Digital Manufacturing Equipment and Technology, School of Mechanical Science and Engineering, Huazhong University of Science and Technology, Wuhan 430074, China

Springer Open

© The Author(s) 2021. **Open Access** This article is licensed under a Creative Commons Attribution 4.0 International License, which permits use, sharing, adaptation, distribution and reproduction in any medium or format, as long as you give appropriate credit to the original author(s) and the source, provide a link to the Creative Commons licence, and indicate if changes were made. The images or other third party material in this article are included in the article's Creative Commons licence, unless indicated otherwise in a credit line to the material. If material is not included in the article's Creative Commons licence and your intended use is not permitted by statutory regulation or exceeds the permitted use, you will need to obtain permission directly from the copyright holder. To view a copy of this licence, visit http://creativecommons.org/licenses/by/4.0/.

since 1960s [15]. In the early development of this technology, only a linear vibration motion in the nominal cutting direction is practiced in machining, which is named as linear vibration cutting (LVC). In 1994, the elliptical vibration cutting (EVC) was proposed by Shamoto and Moriwaki [16]. As follows, the machining feasibilities of EVC on many brittle materials like silicon [17, 18], reaction-bonded silicon carbide [7], tungsten carbide [19, 20], and harden steel [21] has been verified. During EVC process, the subsurface damage can be effectively suppressed since the transient depth of cut (DOC) is much smaller than the nominal DOC [22]. Besides, because of the separation in each vibration cycle, the contact surfaces between the cutting tool and workpiece are exposed into the surrounding gas or fluid, which dissipates the generated cutting heat. Therefore, cutting tool wear like adhesion and thermo-chemical reaction [23] can be effectively suppressed.

To further improve the machinability of brittle materials, hybrid machining (HM) experiments of combining the thermal and vibration assistant have been conducted [24, 25]. It was found that when cutting Inconel 718 by HM method, the machined surface roughness can be effectively decreased [26]. Through experiments and finite element method (FEM) simulations, a substantial drop of the cutting forces and a superior surface quality of titanium alloys can be achieved during HM process [27]. These results demonstrate the feasibility of HM method in precision machining of brittle materials. However, it is hard to directly observe and measure the physical variables during machining process since the cutting tool vibrates in a high frequency and the deformation zone is at high temperature. Furthermore, in nanometric surface fabricating, the transient material removal thickness usually ranges from sub-nanometers to a few nanometers. Therefore, the traditional continuum representation of the problem such as FEM is questionable since the quantum mechanical effects becomes apparent.

In recent years, molecular dynamics (MD) simulation has been widely applied in investigations of the assistive machining process due to its advantages in studying nanometric cutting process [28–30]. Based on previous simulations of TAC [31], when the cutting temperature is increased, the anisotropy in the cutting force, specific cutting energy, and yielding stress becomes more obvious. Meanwhile, the shear force in workpiece is lower at higher cutting temperature, which leads to narrower shear zones and higher magnitudes of the shear plane angle [32]. Furthermore, the material removal rate can be improved with increasing cutting temperature since more chips is formed [33]. For EVC process, it has been discovered by MD simulation that the compressive stress and shear stress in the deformation region can be greatly decreased compared with ordinary cutting [34], which is advantageous for subsurface damage suppression. Besides, EVC process shows obvious thinning of cutting chips, resulting in an increase in the ratio of uncut chip thickness to cut chip thickness [35]. Furthermore, it has been unraveled that the vibration parameters including amplitudes ratios, vibration frequencies, and phase differences have great influences on the material removal performance [34, 36].

These remarkable achievements have improved the understanding of the machining mechanism for assistive machining process. However, in order to save the computation time and memory, the simulation systems are

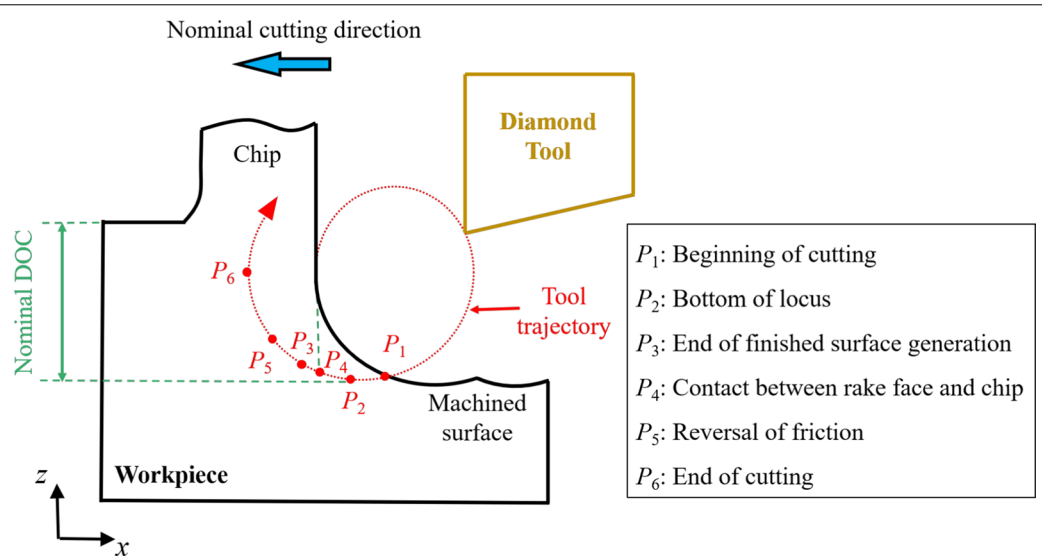

Fig. 1 The schematic diagram of the EVC process

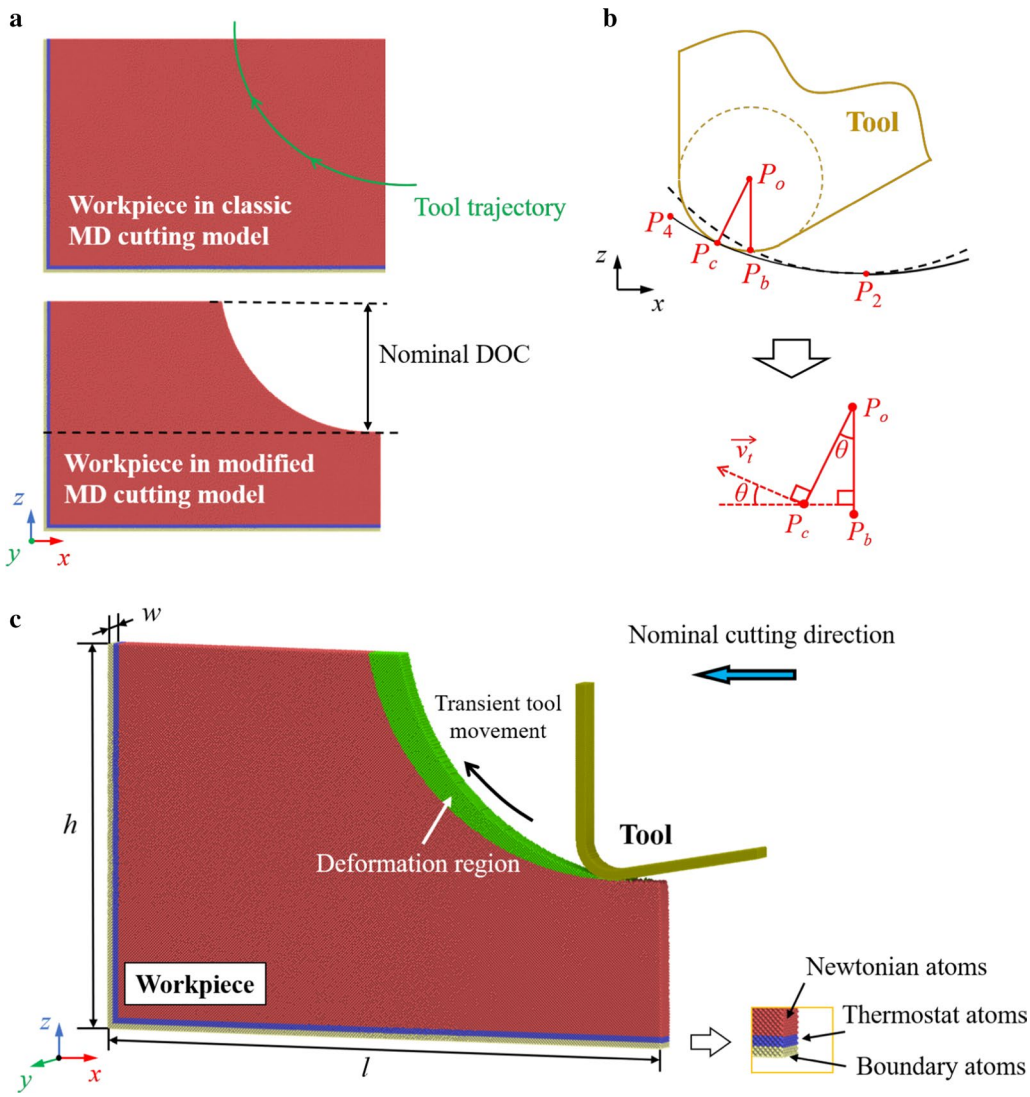

Fig. 2 Scheme of the MD cutting model. **a** Modification of the workpiece. **b** Determination of the tool trajectory. **c** The morphology of the modified MD model. Green atoms represent the deformation region in one vibration cycle

usually quite small. In previous simulations of EVC process, the vibration amplitudes and the nominal DOC are less than 5 nm [22, 36]. Therefore, the transient material removal thickness is usually less than 1 nm, which fails to describe the actual material removal process accurately. Moreover, the MD simulations of the HM process has not been reported. The mechanism of the material removal process and subsurface damage formation during HM process is still unclear. Therefore, in this paper, MD simulation is carried out to reveal the cutting mechanism of HM process. The classic cutting model is modified that the vibration parameters are much closer to the experimental values, e.g., the vibration amplitude is enlarged to 40 nm with a nominal cutting speed of 3.125 m/s. The material removal mechanism in one vibration cycle and the influence of increased cutting temperature are investigated. MD simulation is conducted by the famous Large-scale Atomic/Molecular Massively Parallel Simulator (LAMMPS) [37]. The post processing software OVITO [38] is employed to analyze the simulation results.

Simulation Method

Details of the Cutting Model

Figure 1 shows the schematic diagram of the EVC process, which is originally presented by Shamoto et al. [39]. The tool trajectory can be expressed as:

Table 1 Parameters of the MD simulation model

Parameters	Value
Length l	108.6 nm
Height h	70.6 nm
Width w	4.3 nm
Nominal cutting direction	(001)/[$\bar{1}$00]
Tool rake/clearance angle	0°/10°
Total atoms in workpiece	1,327,001
Phase difference φ	90°
Amplitude in the nominal cutting direction A_c	40 nm
Amplitude in the DOC direction A_d	40 nm
Nominal DOC	40 nm
Vibration frequency f	500 MHz
Nominal cutting speed	3.125 m/s
Tool edge radius	7.14 nm
Ambient temperature	300 K, 600 K, 900 K, 1200 K
Timestep	1 fs

Table 2 Comparison between the parameters between classic model and modified model

Parameters	Experiments [42, 43]	Classic model [22, 36, 44]	Modified model
Vibration amplitude	> 500 nm	< 5 nm	40 nm
Nominal DOC	~ 100 nm	< 5 nm	40 nm
Nominal cutting speed	~ 0.01 m/s	> 50 m/s	3.125 m/s
Vibration frequency	~ 50 kHz	> 10 GHz	500 MHz

$$x(t) = A_c \sin\left(2\pi ft\right) - vt \tag{1}$$

$$z(t) = A_d \sin\left(2\pi ft + \varphi\right) \tag{2}$$

where $x(t)$ and z (t) represent the cutting tool displacement in the x and z directions. A_c and A_d are the vibration amplitude in the nominal cutting direction (x direction) and the nominal DOC direction (negative z direction). Parameters f, v, ϕ, and t represent the vibration frequency, nominal cutting speed, phase difference, and simulation time, respectively. The simulation time t_i represents the time of the point P_i on the tool trajectory from Fig. 1.

According to the geometrical relationship [40], the value of t_1 and t_3 can be determined by:

$$x(t_1) - x(t_3) = 2\pi v/\omega \tag{3}$$

$$z(t_1) - z(t_3) = 0 \tag{4}$$

Then, t_6 can be obtained when the transient movement direction of the diamond tool is parallel to tool rake face:

$$\frac{A_c \sin(2\pi ft_6) + v}{A_d \sin(2\pi ft_6 + \varphi)} = \tan\gamma \tag{5}$$

where γ is the rake angle of diamond cutting tool.

The MD model is present in Fig. 2. The single-crystal silicon workpiece is set as deformable body. While the diamond tool is regarded as rigid body since the tool wear can be neglected in this simulation. The morphology of workpiece in the classic cutting model is reshaped according to tool trajectory in the previous vibration cycle with consideration of the tool edge radius. The tool trajectory can be determined as illustrated in Fig. 2b. P_o and P_b are the center and the bottom point of the tool edge circle. When the tool edge effect is considered, the transient surface generation point P_c varies along the tool edge during the tool movement. The actual finished surface is generated by the envelope line of the cutting tool edge. If the trajectory of P_b is expressed by Eqs. (1) and (2), the trajectory of P_c can be calculated through [41]:

$$x_c(t) = A_c \sin\left(2\pi ft\right) - vt - r\sin\theta(t) \tag{6}$$

$$z_c(t) = A_d \sin\left(2\pi ft + \varphi\right) + r(1 - \cos\theta(t)) \tag{7}$$

where

$$\sin\theta(t) = \frac{z'(t)}{\sqrt{x'(t)^2 + z'(t)^2}} \tag{8}$$

$$\cos\theta(t) = \frac{-x'(t)}{\sqrt{x'(t)^2 + z'(t)^2}} \tag{9}$$

Silicon atoms are divided into three groups: boundary atoms, thermostat atoms, and Newtonian atoms. The boundary atoms are fixed in their balanced positions to hold the workpiece during simulation. The thermostat atoms are kept at the ambient temperature to dissipate the generated cutting heat while Newtonian atoms follow the Newton's second law.

Details of the simulation parameters are listed in Table 1. The length l and height h were determined to keep enough distance between the cutting zone and the fixed boundaries. The periodic boundary condition is applied along the y direction to mimic bulk silicon. The nominal cutting direction, tool rake/clearance angle, and phase difference were determined referring to the experimental setup [42]. The vibration amplitude and

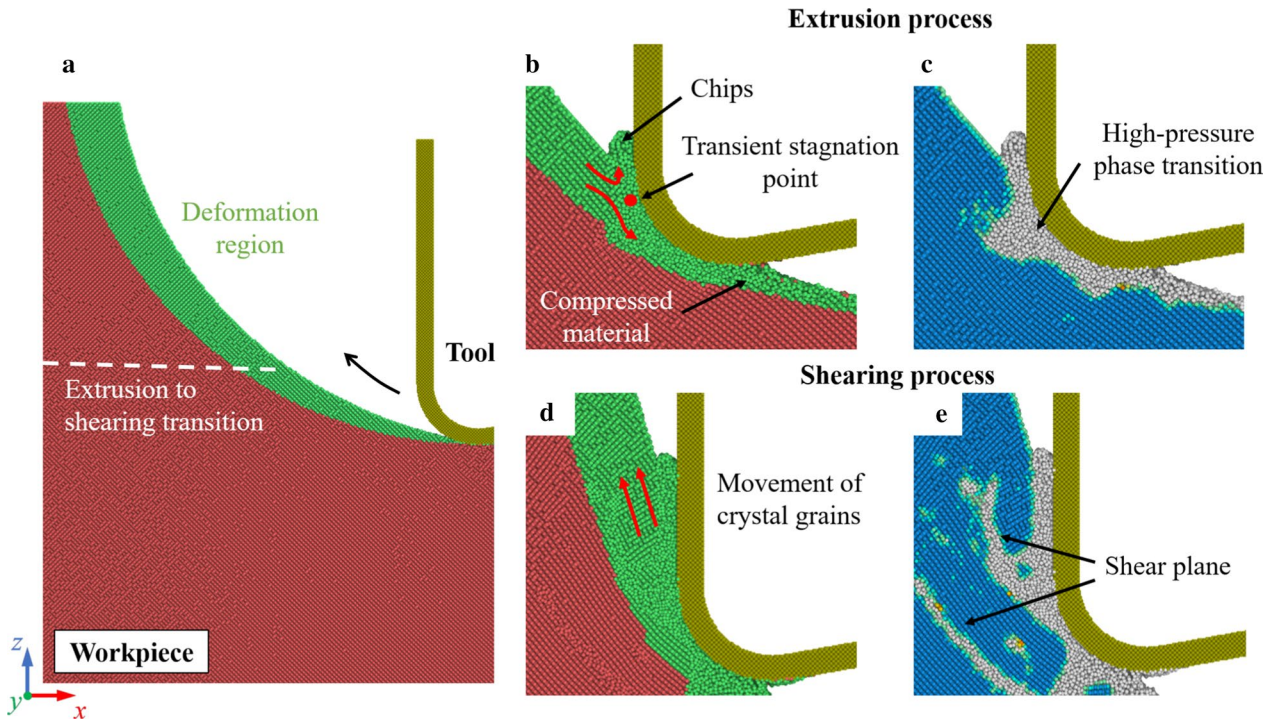

Fig. 3 Transition of the material removal mechanism. **a** Illustration of the deformation region. **b**, **d** Extrusion and shearing process. **c**, **e** Identification of the crystal structure in workpiece. Blue atoms represent the cubic diamond structure while the gray atoms are in the non-diamond structure

nominal DOC are enlarged to approach the experimental scale with acceptable simulation cost. Meanwhile, in order to ensure the thickness of removed material (green atoms in Fig. 2c), the speed ratio and the vibration frequency were set as 40 and 500 MHz, respectively. Therefore, the nominal cutting speed was determined as 3.125 m/s. Furthermore, simulations with different cutting temperature are conducted to reveal the effect of thermal assistant on cutting mechanism. The cutting temperature is increased from 300 to 1200 K, which is realizable during TAC like laser assisted machining [4, 11].

In this modified model, only the cutting stage during the vibration cycle is simulated and the timesteps when the workpiece is separated with cutting tool are saved. Therefore, the computation power can be concentrated on the transient cutting process. Most importantly, the transient material removal process can be described accurately. A comparison between the modified model and classic MD model is shown in Table 2.

Potential Function

In MD simulation, it is important to adopt a robust potential to describe the interaction between atoms. For single-crystal silicon, scholars have developed many potentials such as the modified embedded-atom method (MEAM) [45], Stillinger–Weber (SW) [46], Tersoff [47] and charge optimized many-body (COMB) [48] potentials. Among these potentials, the analytical bond-order potential (ABOP) proposed by Erhart and Albe [49] has attracted growing attention. It is a three-body potential function which allows formation and breaking of bonds during the machining simulation. According to previous researches [50], the ABOP can describe both dimer and bulk properties of silicon accurately. Meanwhile, the mechanical properties of silicon made by the ABOP are consistent with the experiments well [31], which is important in MD simulations of nanoscale machining. Therefore, in this paper, the ABOP potential is applied to describe the silicon–silicon and carbon–carbon interactions. Meanwhile, the interaction of silicon-carbon is described by the Morse potential, which has been proved as an efficient potential in nanoscale cutting simulation [51, 52]. The Morse potential function can be expressed as:

$$E_{\mathrm{Si-C}}(r_{ij}) = D_{\mathrm{M}}\left[\mathrm{e}^{-2a(r_{ij}-R_{\mathrm{M}})} - 2\mathrm{e}^{-a(r_{ij}-R_{\mathrm{M}})}\right] \quad (10)$$

where D_{M}, a, and R_{M} represents the cohesion energy, modulus of elasticity, and the equilibrium distance between atoms, respectively. The parameters for Morse

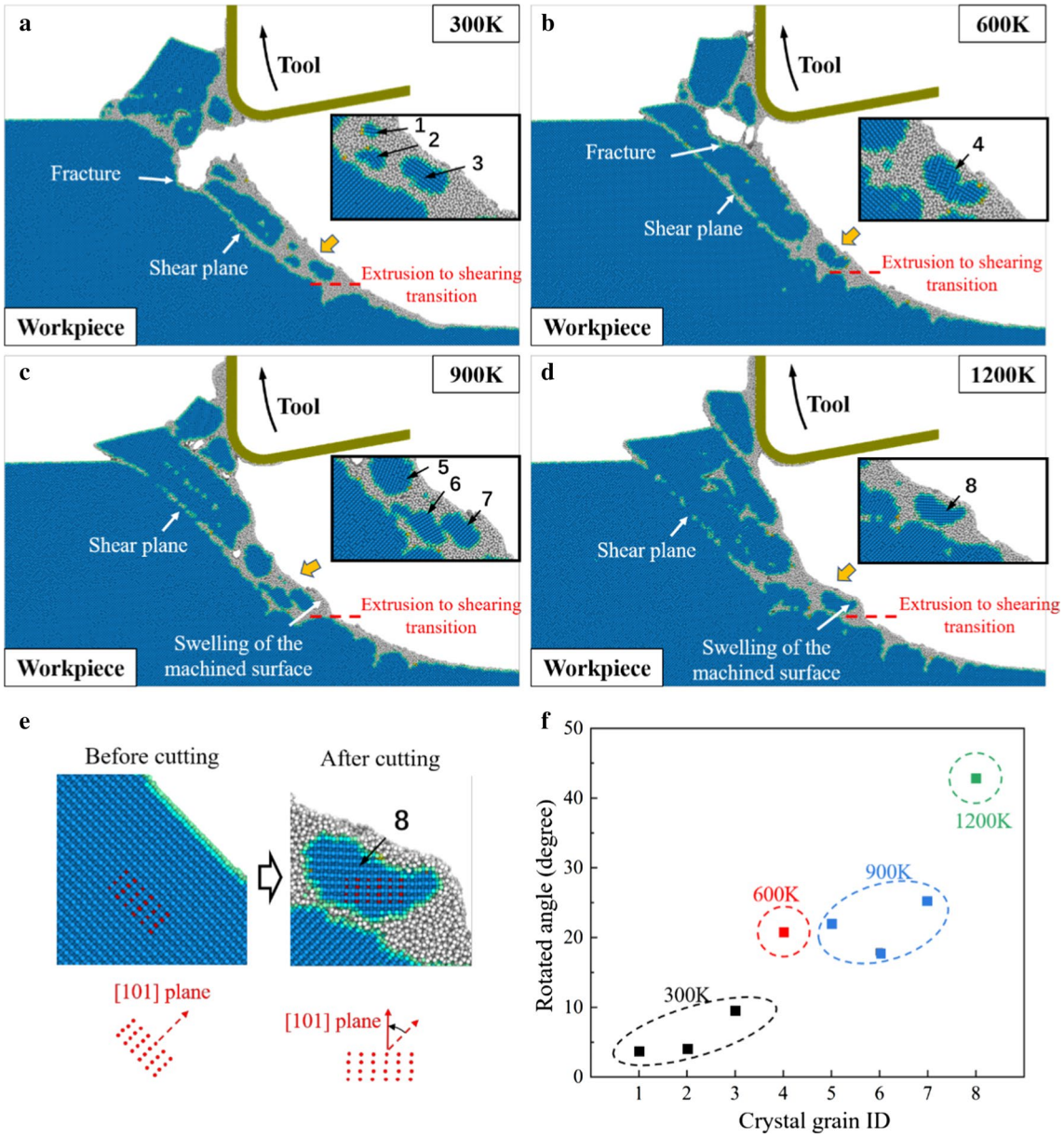

Fig. 4 Workpiece morphology of the HM process at **a** 300 K. **b** 600 K. **c** 900 K. **d** 1200 K. Blue atoms represent the cubic diamond structure while the gray atoms are in non-diamond structure. **e** Determination of the rotation angle of crystal grains. **f** The rotation angle with increasing cutting temperature

potential is [53]: $D_M = 0.435$ eV, $a = 46.487$ nm^{-1}, $R_M = 0.19475$ nm.

Results and Discussion

Cutting Performance

In ordinary cutting, the dominant material removal mechanism can be greatly influenced by the undeformed chip thickness [54]. With small undeformed chip thickness, the dominant material removal mechanism is extrusion. The metallic stable phase (Si-II) can be generated by the high-pressure phase transition (HPPT), which facilities the ductile deformation of silicon. When the undeformed chip thickness is increased, material can be mainly removed via shearing process. While in EVC process, since the undeformed chip thickness is constantly varying, the material removal mechanism can transform from extrusion to shearing in one vibration cycle. Figure 3 shows the snapshots of the cutting simulation

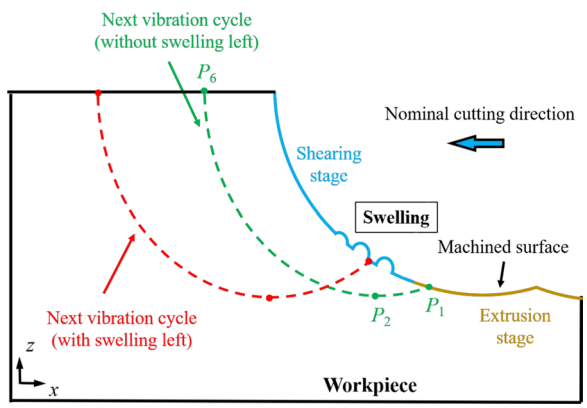

Fig. 5 Elimination of swelling in HM process

at 300 K. The crystal structure of workpiece is determined by the common neighbor analysis (CNA) [55]. This analysis finds atoms that are arranged in a cubic or hexagonal diamond lattice. The non-diamond structure in Fig. 3c, e mainly contains the amorphous phase (a-Si), Si-II, and other defective atoms [56]. These structures are unstable and will transform into a-Si after cutting. It can be observed from Fig. 3b, c that material is mainly removed through extrusion in the initial cutting stage. A transient stagnation point can be observed near the cutting tool edge. Similar with ordinary cutting, materials in the deformation region is divided by the stagnation point into chips and compressed material. As the cutting tool proceeding, the undeformed chip thickness is increased. Shear planes and polycrystal grains are generated in the workpiece, indicating that shearing becomes the dominant material removal mechanism.

Figure 4 shows the workpiece morphology at different cutting temperatures. At 300 K, obvious crack and fracture can be observed in workpiece during the tool upward movement. For brittle material like single-crystal silicon, the tool upward movement would lead to tearing off of materials and leave defects in the workpiece, which is considered as a specific problem in EVC [42]. Although these cracks can be removed by further vibration cycles, the machining stability will be impacted due to the irregularity of workpiece surface. When the cutting temperature is increased, the generation and propagation of cracks is effectively suppressed. From Fig. 4d, no obvious fracture is detected when the cutting temperature raises to 1200 K. However, it is observed that at 900 K and 1200 K, swelling of the machined surface becomes obvious when the material removal mechanism transformed into shearing. It can be concluded that as more crystal grains are generated in shearing stage, the swelling can be caused by the rotation of these crystal grains at high temperature.

For a clear description of this rotation, the coordinates of 24 marked atoms (red atoms) in the crystal grains are used to calculate the average rotation angle, as illustrated in Fig. 4e. The rotation angle of 8 crystal grains (numbered in Fig. 4a–d) is summarized in Fig. 4f. It can be observed that the rotation angle is obviously increased at elevated temperature. During the HM process, the viscosity of a-Si can be greatly decreased at high temperature and the pulling-up motion of workpiece atoms are promoted by the tool upward movement. Therefore, the atomic flow in workpiece is enhanced and the rotation of the crystal grains can be facilitated, leading to swelling of the machined surface. To restrain the rotation of crystal grains, the heating power should be controlled to avoid overheating of the workpiece. Besides, the vibration parameters should be chosen carefully, e.g., smaller nominal cutting speed and higher vibration frequency should be applied to suppress the generation of crystal grains and remove the swelling by further vibration cycles. As illustrated in Fig. 5, with appropriate vibration parameters, P_1 could locate in the extrusion stage and the final machined surface is generated through extrusion without swelling.

Stress Field in Workpiece

To further investigate the cutting mechanism during HM process, the stress distribution in workpiece was calculated. In MD simulation, the hydrostatic stress can be expressed as:

$$\sigma_{\text{hydrostatic}} = (\sigma_x + \sigma_y + \sigma_z)/3 \tag{11}$$

where σ_x, σ_y, and σ_z, are stress tensors from LAMMPS output data.

The hydrostatic stress distribution during extrusion and shearing stages is shown in Fig. 6. And the peak values of the stresses in the compressive and tensile regions were marked. With the tool movement, the contact point between tool and workpiece varies along the tool edge cycle, which results in the movement of the compressive region from the tool edge to the rake face. Following previous reports, the HPPT from single-crystal silicon phase (Si-I) to Si-II could occur at pressures starting at 10–12 GPa [57, 58]. In the cutting simulation at 300 K, the max compressive stress in extrusion and shearing stage reached to 18.1 GPa and 17.6 GPa, respectively. This result indicates that the ductile Si-II phase can be generated during cutting and the HPPT still exists in the shearing stage. In addition, in the extrusion stage, the tensile stress mainly concentrates near the contact area between the tool flank face and machined surface as the

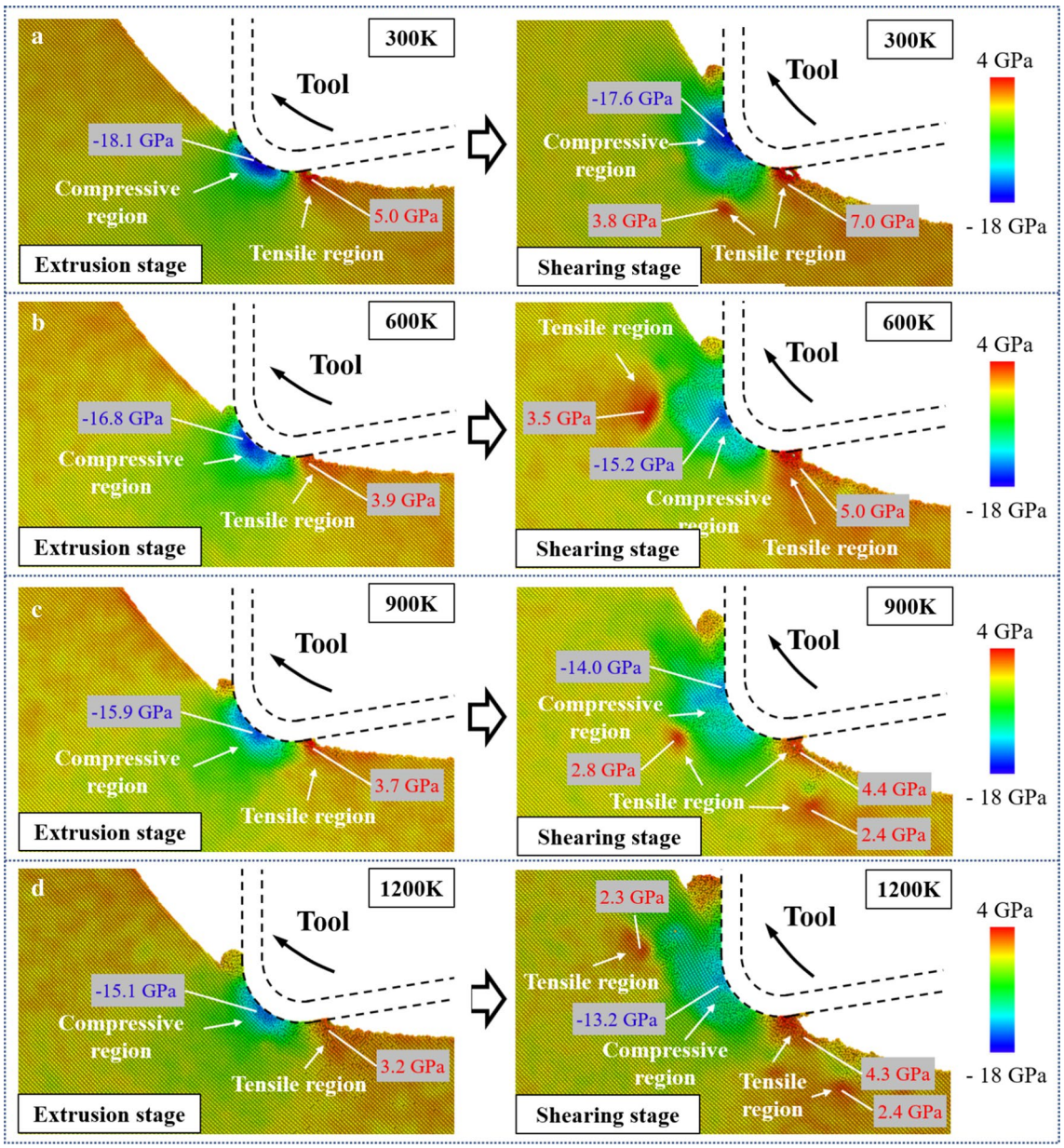

Fig. 6 The hydrostatic stress distribution at: **a** 300 K. **b** 600 K. **c** 900 K. **d** 1200 K

result of the adhesion of silicon atoms and tool surface. As tool proceeds into shearing stage, the tensile region is enlarged and the tensile stress concentration in the subsurface workpiece is greatly increased, which is caused by the pulling-up motion. When the cutting temperature is increased, the plastic deformability of single-crystal silicon is improved and internal stress in the workpiece is decreased. As the temperature increases from 300 to 1200 K, the max compressive stress decreased 16.6% and 25% in extrusion and shearing stage. Meanwhile, although the tensile stress concentration in the subsurface workpiece is still obvious, the peak value of the tensile stress is apparently decreased for more than 30%. It has been reported that the fracture toughness of single-crystal silicon can be effectively increased at higher temperature [59]. Therefore, cracks and fractures caused by the torn-off effect due to tool upward movement can be effectively suppressed.

Single-crystal silicon has a Face Center Cubic (FCC) crystal structure with 12 slip systems. Based on the tool

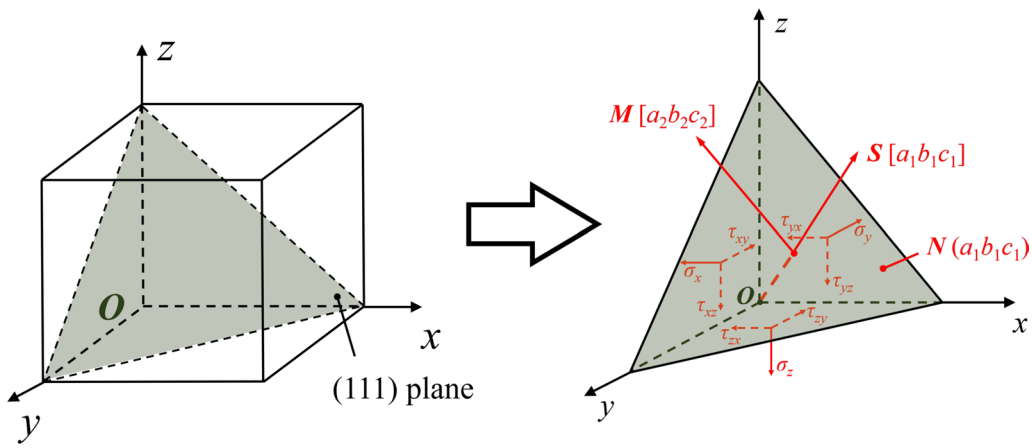

Fig. 7 Illustration of the stress tensors

movement, the main slip systems for shear deformation are the (111)/[$\bar{1}$01] and (111)/[$\bar{1}$01] systems. Therefore, the resolved shear stress component τ_s in the (111)/[$\bar{1}$01] slip system is calculated. As illustrated in Fig. 7, the resolved shear stress component τ_s in the direction $\boldsymbol{M}$ of the slip plane $\boldsymbol{N}$ can be calculated through stress tensors by:

$$\tau_s = a_1a_2\sigma_x + b_1b_2\sigma_y + c_1c_2\sigma_z + (a_1b_2 + a_2b_1)\tau_{xy} + (a_1c_2 + a_2c_1)\tau_{xz} + (b_1c_2 + b_2c_1)\tau_{yz} \quad (12)$$

where a_1, b_1, c_1 are the direction cosines of the normal direction of plane $\boldsymbol{N}$ while a_2, b_2, c_2 are the direction cosines of the slip direction $\boldsymbol{M}$. While τ_{xy}, τ_{xz}, and τ_{yz} are the shear stress tensors from LAMMPS output data.

The distribution of the resolved shear stress τ_s is shown in Fig. 8. The region with positive τ_s is defined as the shear region since the slip motion along the [$\bar{1}$01] direction is promoted, which facilitates the material removal through shearing. While the region with negative τ_s is regarded as the damage region because the slip motion is preferable in the oppose direction, leading to the formation of subsurface damage in workpiece. In the extrusion stage, the stress in the shear region is smaller than that in the damage region. Subsurface damage caused by shear deformation can be generated beneath the machined surface [60]. As the cutting tool movement, the shear stress along the [$\bar{1}$01] direction is gradually increased, causing the material removal transition from extrusion to shearing. Besides, since the position of the damage region moves upward along the tool movement, the generated damage can be removed through further vibration cycle and will not left in workpiece. When the temperature is increased from 300 K to 1200 K, the shear stress in the damage region decreased 36.1% and 42.4% in the extrusion and shearing stage, respectively. In contrast, due to the tool upward motion, the decrease of the shear stress along the [$\bar{1}$01] direction in shearing stage is much less apparent. The critical resolved shear stress (CRSS) for slip motion can be expressed as [61]:

$$\tau_c(T) = C\varepsilon^{1/n}\exp\left(\frac{U}{nkT}\right) \quad (13)$$

where U and ε represent the activation energy of glide movement and the strain rate. Parameters n and C are material constants. It can be concluded that the CRSS can be decreased obviously with increasing temperature. Therefore, the shear deformation in the [$\bar{1}$01] direction can be facilitated at elevated temperature.

Phase Transition

When the cutting temperature is increased, the phase transition of silicon can be greatly influenced. The relaxation of the a-Si and transition to Si-I can be promoted at an appropriate temperature [62]. In Fig. 4, the damage pattern in the workpieces becomes narrower at high temperature. A detailed observation of the damage pattern when cutting at 1200 K is present in Fig. 9a. It is observed that the generated damage in the deformation region is partly recovered after cutting, indicating that the transition from the non-diamond structure to Si-I has occurred. And more Si-I atoms are generated when the cutting temperature is increase, as shown in Fig. 9b. Furthermore, the constructed surface mesh (red color) [63] of the machined workpiece at 1200 K is present in Fig. 9c. It is observed that some vacancies are formed in the subsurface workpiece. Since the atoms are more tightly packed in Si-I phase, the transition to Si-I could

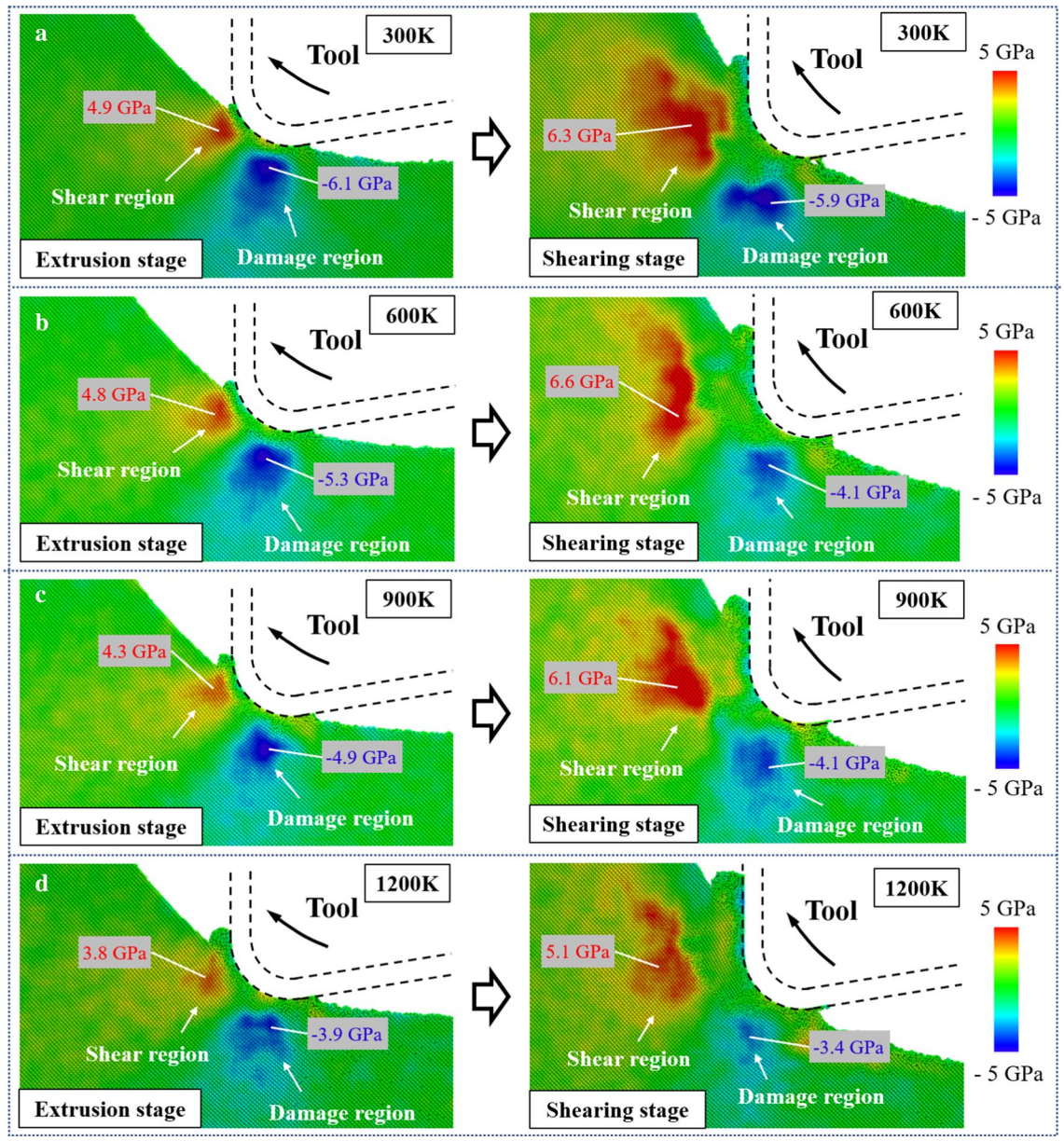

Fig. 8 The resolved shear stress distribution at: **a** 300 K. **b** 600 K. **c** 900 K. **d** 1200 K

cause a shrink of the material, which induces vacancies in workpiece. The volume of the vacancies at different temperatures is calculated and present in Fig. 9d. It is observed that nearly no vacancies are generated at room temperature. While obvious increase of the vacancies can be detected when the cutting temperature is increases to 900 K and 1200 K.

Further analysis of the vacancies is present in Fig. 10. A material element beneath the machined surface is chosen to monitor the vacancies generation. The number of atoms in non-diamond structure and stress evolution of the material element are present. It is concluded that during the cutting process, the material element is firstly compressed and then experiences tensile stress due to the tool upward movement. Meanwhile, two peaks of the shear stress can be observed at 300 K since the shear stress in the damage region is increased as cutting tool passed. When the cutting temperature is increased,

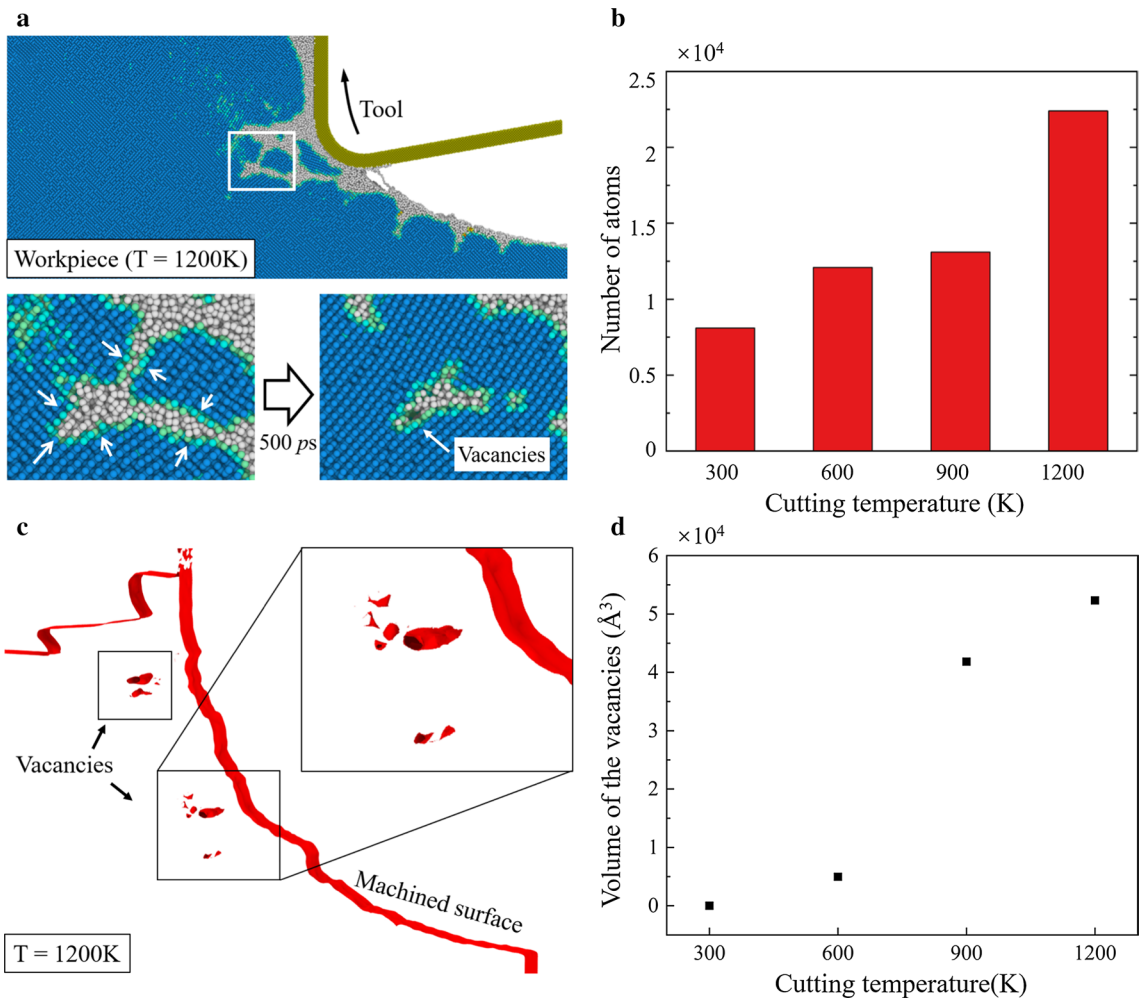

Fig. 9 Relaxation process and vacancies in workpiece. **a** Snapshot of the damage pattern of workpiece at 1200 K. **b** Number of the atoms transformed from the non-diamond structure into Si-I phase. **c** Constructed surface mesh of the workpiece at 1200 K. **d** The volume of the vacancies at different temperatures

the decrease of the shear stress is more obvious than tensile stress. At 1200 K, the second peak of the shear stress is nearly disappeared while tensile stress becomes dominant in the material element during the relaxation process.

To explore the effect of tensile stress on formation process of the vacancies, relaxation simulations of bulk silicon sample were conducted. As shown in Fig. 11a, the initial model composes of 40% Si-I atoms and 60% a-Si atoms, which is generated by the melting-quench method [64]. The size of the model is 21.7 nm × 8.1 nm × 26.1 nm in x, y, and z direction, which contains 230,400 atoms. The initial interface between crystal and non-crystal region is set as (001) crystal plane. Periodic boundary condition is applied in three dimensions to mimic bulk materials. The constructed surface mesh of the relaxed model is present in Fig. 11b. Furthermore, to quantify the vacancies, the solid volume fraction is calculated as the ratio of the solid material volume and the total volume of the simulation sample, as shown in Fig. 11c. It is observed that when temperature is increased, the solid volume fraction decreased obviously under tensile stress. Therefore, to suppress the vacancies, the desired cutting temperature in HM process should be lower than that in ordinary TAC. Meanwhile, the vibration parameters should be optimized to reduce the tensile stress in subsurface workpiece.

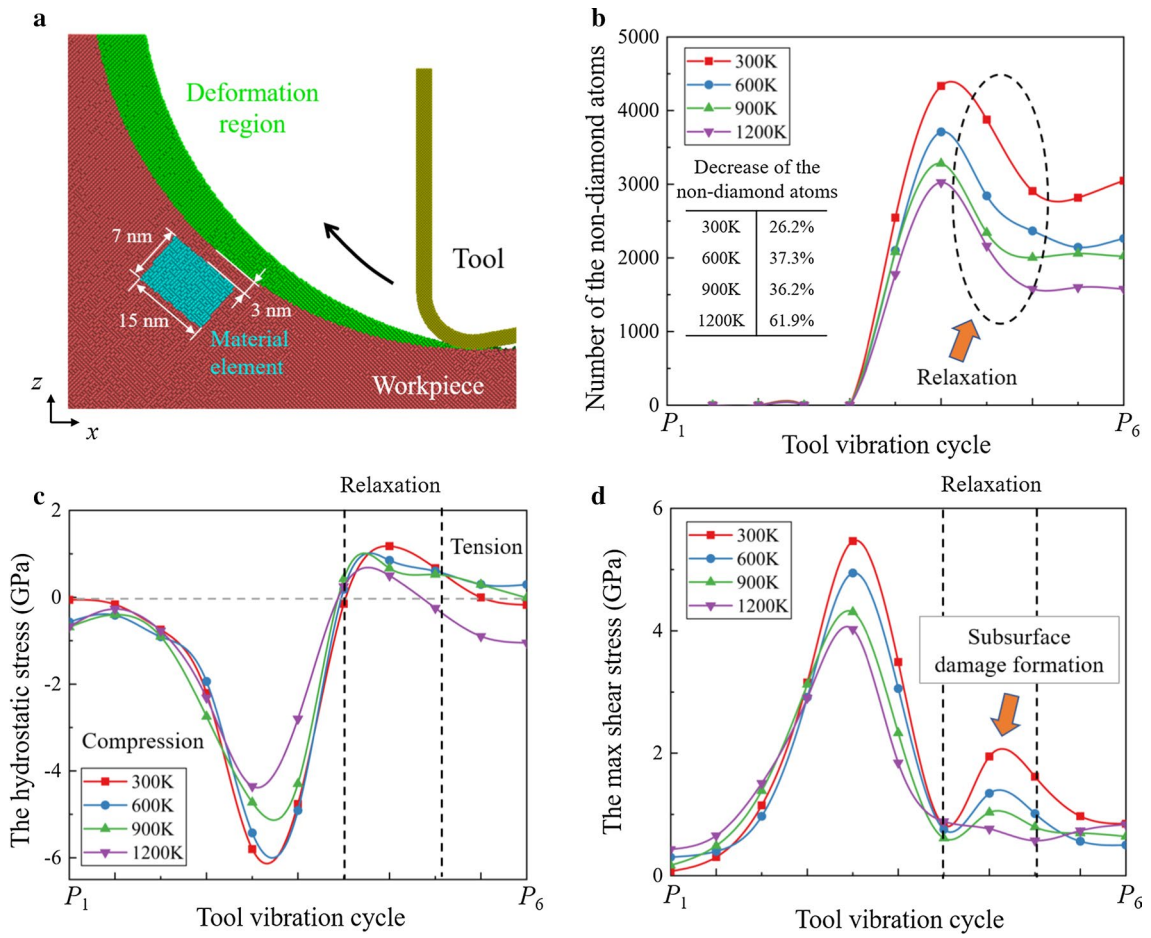

Fig. 10 Relaxation during the HM process. **a** Illustration of the material element. **b** Statistics of the atoms in non-diamond structure in the material element. **c**, **d** Stress evolution of the material element

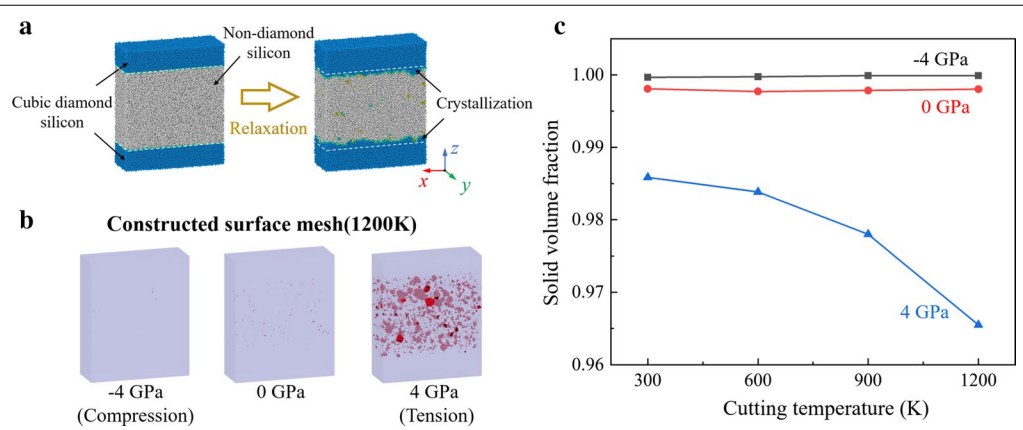

Fig. 11 Relaxation simulation of silicon. **a** Scheme of MD relaxation simulation. **b** The surface mesh of the relaxed model at 1200 K. **c** The solid volume fraction curves

Conclusions

In this paper, MD simulation is carried out to investigate the cutting mechanism of hybrid machining (HM) process. A modified cutting model is applied to reveal the material removal behavior and subsurface damage formation in one vibration cycle. The main conclusions were as follows:

(1) During HM process, the dominant material removal mechanism could transform from extrusion to shear in a single vibration cycle. With an increase of the cutting temperature, the generation and propagation of cracks can be effectively suppressed. However, the swelling appears when the dominant material removal mechanism becomes shearing, which is caused by the rotation of the crystal grains in workpiece.

(2) Based on the stress analysis, the dominant formation mechanism of the subsurface damage in one vibration cycle can be distinct. In the extrusion stage, the subsurface damage can be generated by the shear stress in the damage region. While in the shearing stage, tensile stress becomes dominant in subsurface damage formation. When the cutting temperature is increased, although the tensile stress concentration in the subsurface workpiece is still obvious, the peak value of the stresses is apparently decreased, which effectively suppress the cracks and fractures in workpiece.

(3) When the cutting temperature is increased, less subsurface damage is generated in the workpiece. However, due to the tensile stress, some vacancies can be generated in the workpiece when the cutting temperature is increased. Therefore, the desired cutting temperature during HM process should be lower than that in ordinary TAC and the vibration parameters should be set carefully to suppress the vacancies in the subsurface workpiece.

Abbreviations

TAC: Thermal assisted cutting; VAC: Vibration assisted cutting; LVC: Linear vibration cutting; EVC: Elliptical vibration cutting; DOC: Depth of cut; HM: Hybrid machining; FEM: Finite element method; MD: Molecular dynamics; LAMMPS: Large-scale Atomic/Molecular Massively Parallel Simulator; MEAM: Modified embedded-atom method; SW: Stillinger–Weber; COMB: Charge optimized many-body; ABOP: Analytical bond-order potential; Si-II: Metallic stable phase; HPPT: High-pressure phase transition; CNA: Common neighbor analysis; a-Si: Amorphous phase; Si-I: Single-crystal silicon phase; FCC: Face Center Cubic; CRSS: Critical resolved shear stress.

Acknowledgements

The authors gratefully acknowledge Xi Zhang for providing help in data analysis.

Authors' contributions

CL carried out the MD simulations and drafted the manuscript. WH and XC participated in conducting the MD simulation. JC and JZ participated in the design of the study. JX (Junfeng Xiao) and JX (Jianfeng Xu) conceived of the study and helped to draft the manuscript. All authors read and approved the final manuscript.

Funding

Jianguo Zhang is grateful for the part of original support from the National Natural Science Foundation of China (No. 51905194), the Wuhan Science and Technology Plan in China (No. 2019010701011400) and the Key Laboratory for Precision and Non-traditional Machining Technology in Dalian University of Technology (B201901). Jianfeng Xu acknowledge the support from the National Natural Science Foundation of China (51627807).

Availability of data and materials

The datasets used and analyzed in the current study can be obtained from the corresponding authors upon reasonable request.

Declaration

Competing interests

The authors declare no competing interests.The authors declare no competing interests.

Received: 11 January 2021 Accepted: 12 April 2021
Published online: 21 April 2021

References

1. Zong WJ, Sun T, Li D, Cheng K, Liang YC (2008) XPS analysis of the groove wearing marks on flank face of diamond tool in nanometric cutting of silicon wafer. Int J Mach Tools Manuf 48:1678–1687
2. Kang Q, Fang X, Sun L, Ding J, Jiang Z (2019) Research on mechanism of nanoscale cutting with arc trajectory for monocrystalline silicon based on molecular dynamics simulation. Comput Mater Sci 170:109175
3. Huo D, Lin C, Choong ZJ, Pancholi K, Degenaar P (2015) Surface and subsurface characterisation in micro-milling of monocrystalline silicon. Int J Adv Manuf Technol 81:1319–1331
4. Chen X, Liu C, Ke J, Zhang J, Shu X, Xu J (2020) Subsurface damage and phase transformation in laser-assisted nanometric cutting of single crystal silicon. Mater Des 190:108524
5. Yan J, Asami T, Harada H, Kuriyagawa T (2009) Fundamental investigation of subsurface damage in single crystalline silicon caused by diamond machining. Precis Eng 33:378–386
6. Kim JD, Lee SJ, Suh J (2011) Characteristics of laser assisted machining for silicon nitride ceramic according to machining parameters. J Mech Sci Technol 25:995–1001
7. Zhang J, Han L, Zhang J, Liu H, Yan Y, Sun T (2019) Brittle-to-ductile transition in elliptical vibration-assisted diamond cutting of reaction-bonded silicon carbide. J Manuf Process 45:670–681
8. Ding H, Shin YC (2012) Improvement of machinability of Waspaloy via laser-assisted machining. Int J Adv Manuf Technol 64:475–486
9. Mohammadi H, Poyraz HB, Ravindra D, Patten JA (2015) Surface finish improvement of an unpolished silicon wafer using micro-laser assisted machining. Int J Abras Technol 7:107–121
10. Mohammadi H, Ravindra D, Kode SK, Patten JA (2015) Experimental work on micro laser-assisted diamond turning of silicon (111). J Manuf Process 19:125–128
11. Ravindra D, Ghantasala MK, Patten J (2012) Ductile mode material removal and high-pressure phase transformation in silicon during micro-laser assisted machining. Precis Eng 36:364–367
12. Ruffell S, Bradby JE, Williams JS, Munoz-Paniagua D, Tadayyon S, Coatsworth LL, Norton PR (2009) Nanoindentation-induced phase transformations in silicon at elevated temperatures. Nanotechnology 20:135603

13. Langan SM, Ravindra D, Mann AB (2018) Process parameter effects on residual stress and phase purity after microlaser-assisted machining of silicon. Mater Manuf Process 33:1578–1586
14. Shore P, Cunningham C, DeBra D, Evans C, Hough J, Gilmozzi R, Kunzmann H, Morantz P, Tonnellier X (2010) Precision engineering for astronomy and gravity science. CIRP Ann Manuf Technol 59:694–716
15. Skelton RC (1968) Turning with an oscillating tool. Int J Mach Tool Des Res 8:239–259
16. Shamoto E, Moriwaki T (1994) Study on elliptical vibration cutting. CIRP Ann Manuf Technol 43:35–38
17. Zhang X, Arif M, Liu K, Kumar AS, Rahman M (2013) A model to predict the critical undeformed chip thickness in vibration-assisted machining of brittle materials. Int J Mach Tools Manuf 69:57–66
18. Wang J, Yang Y, Guo P (2018) Effects of vibration trajectory on ductile-to-brittle transition in vibration cutting of single crystal silicon using a non-resonant tool. Procedia CIRP 71:289–292
19. Nath C, Rahman M, Neo KS (2009) Machinability study of tungsten carbide using PCD tools under ultrasonic elliptical vibration cutting. Int J Mach Tools Manuf 49:1089–1095
20. Suzuki N, Hino R, Masuda S, Shamoto E (2006) Ultraprecision cutting of sintered tungsten carbide by applying elliptical vibration cutting-Study on ductile cutting mechanics. J Jpn Soc Precis Eng 72:539–545 (**in Japanese**)
21. Zhang J, Zhang J, Rosenkranz A, Suzuki N, Shamoto E (2019) Frictional properties of surface textures fabricated on hardened steel by elliptical vibration diamond cutting. Precis Eng 59:66–72
22. Zhu B, Zhao D, Zhao H, Guan J, Hou P, Wang S, Qian L (2017) A study on the surface quality and brittle-ductile transition during the elliptical vibration-assisted nanocutting process on monocrystalline silicon via molecular dynamic simulations. RSC Adv 7:4179–4189
23. Zhang J, Cui T, Ge C, Sui Y, Yang H (2016) Review of micro/nano machining by utilizing elliptical vibration cutting. Int J Mach Tools Manuf 106:109–126
24. Muhammad R, Maurotto A, Roy A, Silberschmidt VV (2012) Hot ultrasonically assisted turning of β-Ti alloy. Procedia CIRP 1:336–341
25. Muhammad R, Maurotto A, Demiral M, Roy A, Silberschmidt VV (2014) Thermally enhanced ultrasonically assisted machining of Ti alloy. CIRP Ann Manuf Sci Technol 7:159–167
26. Hsu CY, Lin YY, Lee WS, Lo SP (2008) Machining characteristics of Inconel 718 using ultrasonic and high temperature-aided cutting. J Mater Process Technol 198:359–365
27. Muhammad R, Ahmed N, Ullah H, Roy A, Silberschmidt VV (2018) Hybrid machining process: experimental and numerical analysis of hot ultrasonically assisted turning. Int J Adv Manuf Technol 97:2173–2192
28. Goel S, Kovalchenko A, Stukowski A, Cross G (2016) Influence of microstructure on the cutting behaviour of silicon. Acta Mater 105:464–478
29. Zhang J, Zheng H, Shuai M, Li Y, Yang Y, Sun T (2017) Molecular dynamics modeling and simulation of diamond cutting of cerium. Nanoscale Res Lett 12:464
30. Wang J, Zhang X, Fang F, Chen R (2018) A numerical study on the material removal and phase transformation in the nanometric cutting of silicon. Appl Surf Sci 455:608–615
31. Chavoshi SZ, Goel S, Luo X (2016) Influence of temperature on the anisotropic cutting behaviour of single crystal silicon: a molecular dynamics simulation investigation. J Manuf Process 23:201–210
32. Chavoshi SZ, Luo X (2016) An atomistic simulation investigation on chip related phenomena in nanometric cutting of single crystal silicon at elevated temperatures. Comput Mater Sci 113:1–10
33. Dai H, Li S, Chen G (2018) Comparison of subsurface damages on mono-crystalline silicon between traditional nanoscale machining and laser-assisted nanoscale machining via molecular dynamics simulation. Nucl Instrum Methods B 414:61–67
34. Liu C, Zhang J, Zhang J, Chen X, Xiao J, Xu J (2020) A simulation investigation on elliptical vibration cutting of single-crystal silicon. Int J Adv Manuf Technol 108:2231–2243
35. Goel S, Martinez FD, Chavoshi SZ, Khatri N, Giusca C (2018) Molecular dynamics simulation of the elliptical vibration-assisted machining of pure iron. J Micromanuf 1:6–19
36. Dai H, Du H, Chen J, Chen G (2019) Influence of elliptical vibration on the behavior of silicon during nanocutting. Int J Adv Manuf Technol 102:3597–3612
37. Plimpton S (1995) Fast parallel algorithms for short-range molecular dynamics. J Comput Phys 117:1–19
38. Alexander S (2010) Visualization and analysis of atomistic simulation data with OVITO-the Open Visualization Tool. Model Simul Mater Sci Eng 18(1):015012
39. Shamoto E, Morimoto Y, Moriwaki T (1999) Elliptical vibration cutting (2nd report, study on effects of vibration conditions). J Jpn Soc Precis Eng 65:411–417 (**in Japanese**)
40. Zhang X (2012) A study of elliptical vibration cutting in ultra precision machining. Ph.D Thesis, National University of Singapore, p 154
41. Zhang X, Kumar AS, Rahman M, Liu K (2013) Modeling of the effect of tool edge radius on surface generation in elliptical vibration cutting. Int J Adv Manuf Technol 65:35–42
42. Zhang J, Zhang J, Cui T, Hao Z, Al Zahrani A (2017) Sculpturing of single crystal silicon microstructures by elliptical vibration cutting. J. Manuf. Process. 29:389–398
43. Wang J, Yang Y, Zhu Z, Wang Y, Liao W-H, Guo P (2020) On ductile-regime elliptical vibration cutting of silicon with identifying the lower bound of practicable nominal cutting velocity. J Mater Process Technol 283:116720
44. Dai H, Chen J, Liu G (2019) A numerical study on subsurface quality and material removal during ultrasonic vibration assisted cutting of monocrystalline silicon by molecular dynamics simulation. Mater Res Express 6:065908
45. Jelinek B, Groh S, Horstemeyer MF, Houze J, Kim SG, Wagner GJ, Moitra A, Baskes MI (2012) Modified embedded atom method potential for Al, Si, Mg, Cu, and Fe alloys. Phys Rev B 85:245102
46. Stillinger FH, Weber TA (1985) Computer simulation of local order in condensed phases of silicon. Phys Rev B 31:5262–5271
47. Tersoff J (1989) Modeling solid-state chemistry: interatomic potentials for multicomponent systems. Phys Rev B 39:5566–5568
48. Shan TR, Devine BD, Kemper TW, Sinnott SB, Phillpot SR (2010) Charge-optimized many-body potential for the hafnium/hafnium oxide system. Phys Rev B 81:125328
49. Erhart P, Albe K (2005) Analytical potential for atomistic simulations of silicon, carbon, and silicon carbide. Phys Rev B 71:035211
50. Goel S, Luo X, Reuben RL, Pen H (2012) Influence of temperature and crystal orientation on tool wear during single point diamond turning of silicon. Wear 284–285:65–72
51. Guo X, Li Q, Liu T, Zhai C, Kang R, Jin Z (2016) Molecular dynamics study on the thickness of damage layer in multiple grinding of monocrystalline silicon. Mater Sci Semicond Process 51:15–19
52. Dai H, Chen G, Zhou C, Fang Q, Fei X (2017) A numerical study of ultraprecision machining of monocrystalline silicon with laser nano-structured diamond tools by atomistic simulation. Appl Surf Sci 393:405–416
53. Cai MB, Li XP, Rahman M (2007) Characteristics of "dynamic hard particles" in nanoscale ductile mode cutting of monocrystalline silicon with diamond tools in relation to tool groove wear. Wear 263:1459–1466
54. Ameli Kalkhoran SN, Vahdati M, Yan J (2020) Effect of relative tool sharpness on subsurface damage and material recovery in nanometric cutting of mono-crystalline silicon: a molecular dynamics approach. Mater Sci Semicond Process 108:104868
55. Maras E, Trushin O, Stukowski A, Ala-Nissila T, Jónsson H (2016) Global transition path search for dislocation formation in Ge on Si(001). Comput Phys Commun 205:13–21
56. Dai H, Zhang F, Zhou Y (2020) Numerical study of three-body diamond abrasive polishing single crystal Si under graphene lubrication by molecular dynamics simulation. Comput Mater Sci 171:109214

57. Sanz-Navarro CF, Kenny SD, Smith R (2004) Atomistic simulations of structural transformations of silicon surfaces under nanoindentation. Nanotechnology 15:692–697
58. Kim DE, Oh SI (2006) Atomistic simulation of structural phase transformations in monocrystalline silicon induced by nanoindentation. Nanotechnology 17:2259–2265
59. Nakao S, Ando T, Shikida M, Sato K (2008) Effect of temperature on fracture toughness in a single-crystal-silicon film and transition in its fracture mode. J Micromech Microeng 18:015026
60. Wang Z, Chen J, Wang G, Bai Q, Liang Y (2017) Anisotropy of single-crystal silicon in nanometric cutting. Nanoscale Res Lett 12:300
61. Lojek B (1993) Issues in manufacturing unique silicon devices using rapid thermal annealing. Rapid Therm Process 1:311–348
62. Xiao Y, Motooka T, Teranishi R, Munetoh S (2013) Nucleation of Si and Ge by rapid cooling using molecular-dynamics simulation. J Cryst Grow 362:103–105
63. Stukowski A (2013) Computational analysis methods in atomistic modeling of crystals. Jom 66:399–407
64. Guo X, Zhai C, Kang R, Jin Z (2015) The mechanical properties of the scratched surface for silica glass by molecular dynamics simulation. J Noncryst Solids 420:1–6

Publisher's Note

Springer Nature remains neutral with regard to jurisdictional claims in published maps and institutional affiliations.

Submit your manuscript to a SpringerOpen journal and benefit from:

- ► Convenient online submission
- ► Rigorous peer review
- ► Open access: articles freely available online
- ► High visibility within the field
- ► Retaining the copyright to your article

Submit your next manuscript at ► springeropen.com